Prediction of O_2 Dissociation Kinetics on $LaMnO_3$-Based Cathode Materials for Solid Oxide Fuel Cells

YongMan Choi,[||,†] Matthew E. Lynch,[†] M. C. Lin,[‡,§] and Meilin Liu*[,†]

Center for Innovative Fuel Cell and Battery Technologies, School of Materials Science and Engineering, Georgia Institute of Technology, Atlanta, Georgia 30332, Department of Chemistry, Emory University, 1515 Dickey Drive, Atlanta, Georgia 30322, and Center for Interdisciplinary Molecular Science, National Chiao Tung University, Hsinchu 30010, Taiwan

Received: December 14, 2008; Revised Manuscript Received: February 21, 2009

First-principles and statistical-theory calculations were applied to examine the interactions between oxygen molecules and the (100) surfaces of $LaMnO_3$ and $La_{0.5}Sr_{0.5}MnO_{2.75}$, one of the most-used cathode materials in solid oxide fuel cells (SOFCs). To predict the rate constants for the interactions between O_2 and $LaMnO_3$ or $La_{0.5}Sr_{0.5}MnO_{2.75}$, potential energy profiles were constructed using the nudged elastic band (NEB) method. Predicted rate constants for the dissociation of adsorbed oxygen species on $LaMnO_3$ (**lm**) and $La_{0.5}Sr_{0.5}MnO_{2.75}$ (**lsm**) can be expressed as $k_{diss,lm} = 2.35 \times 10^{12} \exp(-0.50\ eV/RT)\ s^{-1}$ and $k_{diss,lsm} = 2.15 \times 10^{12} \exp(-0.23\ eV/RT)\ s^{-1}$, respectively, in the temperature range of 873−1273 K at 1 atm. Because the activation energy for oxygen dissociation on $La_{0.5}Sr_{0.5}MnO_{2.75}$ (0.23 eV) is much smaller than that on $LaMnO_3$ (0.50 eV), oxygen vacancies greatly enhance O_2 dissociation kinetics. The kinetic and mechanistic studies for the interactions at the molecular level are imperative to gaining a fundamental understanding of oxygen reduction kinetics on cathode materials and to providing important insight into the rational design of more catalytically active cathode materials for SOFCs.

1. Introduction

While solid oxide fuel cells (SOFCs) are potentially the cleanest, most efficient chemical-to-electrical energy conversion systems with excellent fuel flexibility (i.e., potential for direct utilization of hydrocarbon fuels, coal gas, biomass, and other renewable fuels), rational design of efficient cathode materials for SOFCs remains one of the most critical scientific challenges facing the development of low-cost SOFCs.[1] It is well-known that the polarization resistances due to oxygen reduction on the cathode contribute the most to the loss in energy efficiency of SOFCs, especially at low temperatures (<500 °C).[2] To characterize the surface catalytic properties of cathode materials, a phenomenological parameter called the oxygen surface exchange coefficient (k^*) has been introduced.[3] To date, secondary ion mass spectrometry (SIMS)[4,5] has been widely used to determine k^*.[6,7] On the basis of phenomenological theories, De Souza[5] has recently developed an expression for k^* as a function of defect concentrations (oxygen vacancies, electrons, and electron holes), thermal rate constants, and partial pressure of oxygen. To achieve rational design of efficient cathode materials, however, it is vital to gain a deeper understanding of the inherent correlations between the surface catalytic properties (or k^*) and the chemical composition and structure of the cathode materials. While various electrochemical techniques (e.g., impedance spectroscopy[8] and SIMS) have provided important information about cathode performance, it is extremely difficult, if not impossible, to deduce detailed information on elementary steps involved in the surface processes due to the complexity of the electrochemically active interfaces.[9] First-principles calculations, however, have been successfully used to examine the energetics for the elementary steps involved in oxygen reduction on cathode materials.[10,11] Recently, Kotomin and co-workers[12] presented a systematic study on O−$LaMnO_3$(001) interactions, including defect migration of dissociated oxygen species, using ab initio calculations and the thermodynamic-correction approach. The molecular-level studies provide important insight into the reaction sequence and mechanism on different crystallographic surfaces, as well as its dependence on surface structure and defects (e.g., oxygen vacancies). This information is vital to understanding the catalytic activity of cathode materials, but difficult to obtain by experimental measurements alone. Here, we report O_2 dissociation kinetics for the interactions between oxygen species and $LaMnO_3$-based cathode materials, predicting the rate constants for each elementary step (e.g., adsorption, desorption, and dissociation, as shown in Scheme 1).

2. Computational Methods

All periodic DFT calculations were performed using the Vienna ab initio simulation package (VASP).[13,14] We applied the projector-augmented wave (PAW) method[15] with a 400 eV cutoff energy to represent electron−ion interactions. The generalized gradient approximation with the Perdew−Wang (GGA-PW91) exchange-correlation functional[16] was used. La, Sr, Mn, and O atoms were described by 11 ($5s^25p^65d^16s^2$), 10 ($4s^24p^65s^2$), 7 ($4s^13d^6$), and 6 ($2s^2sp^4$) valence electrons, respectively. To converge the total electronic energy within ~0.01 eV, (4 × 4 × 4) Monkhorst-Pack mesh[17] **k**-points were applied. Similar to our previous studies on the interactions of O_2 on $LaMnO_3$-based cathode materials,[10,11] the cubic perovskite structure of *Pm*3*m* was considered because $LaMnO_3$ has a cubic structure under SOFC operating conditions (above 500 °C in

* Corresponding author. Tel.: (404) 894-6114. Fax: (404) 894-9140. E-mail: meilin.liu@mse.gatech.edu.
† Georgia Institute of Technology.
‡ Emory University.
§ National Chiao Tung University.
|| Present address: Chemistry Department Brookhaven National Laboratory, Upton, NY 11973.

10.1021/jp811021p CCC: $40.75
Published on Web 04/07/2009

SCHEME 1: Schematic of Elementary Reaction Steps of the Interactions between O_2 and $LaMnO_3$[a]

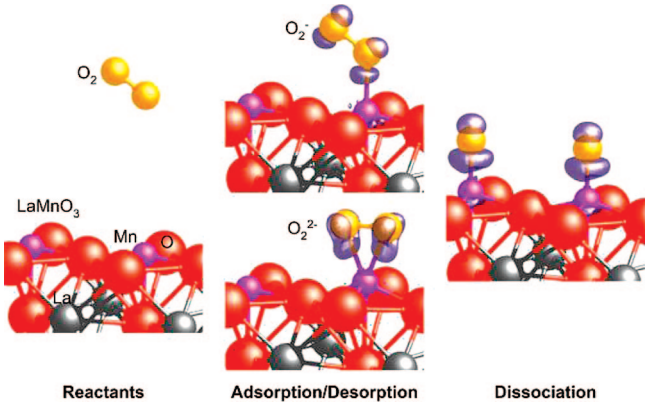

[a] Isosurfaces in purple represent charge-density changes around oxygen species on the surface. O_2^- and O_2^{2-} correspond to superoxo- and peroxo-like species, respectively.

ambient air).[18,19] Accordingly, we generated a cubic-structure Sr-doped $LaMnO_3$ surface model based on undoped $LaMnO_3$. The spin-polarized method was used to properly describe the magnetic property of $LaMnO_3$-based materials and the triplet ground state of oxygen ($^3O_2$). Our previous study[10] demonstrated that the ferromagnetic (FM) configuration of $LaMnO_3$ is approximately 0.5 eV more stable than the antiferromagnetic (AFM) configuration; thus, we carried out DFT calculations only on the FM state. In particular, to elucidate the reaction mechanism for oxygen interactions on the cathode materials, we first mapped out minimum-energy paths (MEPs) using the nudged elastic band (NEB) method[20,21] by connecting reactants, intermediates, or products. The charge-density change was estimated by $\Delta\rho_{diff} = \rho$[adsorbate−substrate] − ρ[adsorbate] − ρ[substrate], while atomic charges were calculated using the Bader analysis code,[22,23] based on Bader's theory of atoms in molecules (AIM).[24,25] We applied the transition state theory (TST) formalism[26] to predict rate constants for adsorption, desorption, and dissociation, and the canonical transition state theory (CVTST) approach[27,28] was utilized to locate transition states for the adsorption/desorption step occurring without a barrier. A more detailed description of its procedure will be discussed in the Results and Discussion. All of the rate constants were evaluated by using the ChemRate program.[29]

Figure 1a represents a schematic of a bulk structure of MnO-terminated $LaMnO_3$. The $LaMnO_3$ supercell contains a total of 20 ions (4 La, 4 Mn, and 12 O ions) as periodically repeated slabs consisting of 4 atomic layers. Calculations produced a bulk lattice constant of 3.876 Å.[30] For the characterization of the O_2−surface interactions, the (100) surface was applied in this study because (100) is the most stable among the low-index (111), (110), and (100) surfaces according to surface-stability calculations.[10,18] Although the $LaMnO_3$(100) surface is composed of LaO- and MnO-terminated surfaces, we only considered the MnO-terminated surface for the surface interactions because it is known that for ABO_3-structure cathode materials, B cations are more active than A cations toward oxygen reduction.[31] Thus, all of DFT calculations were conducted using MnO-terminated (100) surface models as shown in Figure 1b−1e. A systematic construction of Sr-doped surface models (see Figure 1d and 1e) will be discussed in the Results and Discussion.

3. Results and Discussion

3.1. Surface Coverage Effects on $LaMnO_3$. On the basis of the optimized bulk $LaMnO_3$ structure, we examined the surface coverage effects for O−surface interactions using the 2-D slab model calculations. For the surface calculations, slabs were separated by a vacuum space of ∼24 Å in the direction perpendicular to the surface. Similar to our previous study,[10] all surface calculations were performed by relaxing the top two layers while fixing the bottom two layers to the estimated bulk parameters. We then estimated adsorption energies by placing one or two "O" atoms on Mn ions (see the top view in Figure 1b) containing six ions (2 Mn and 4 O ions) on the top layer, leading to the coverage of 1/6 ML and 1/3 ML, respectively. In this study, the adsorption energy for the O−surface interactions is calculated according to

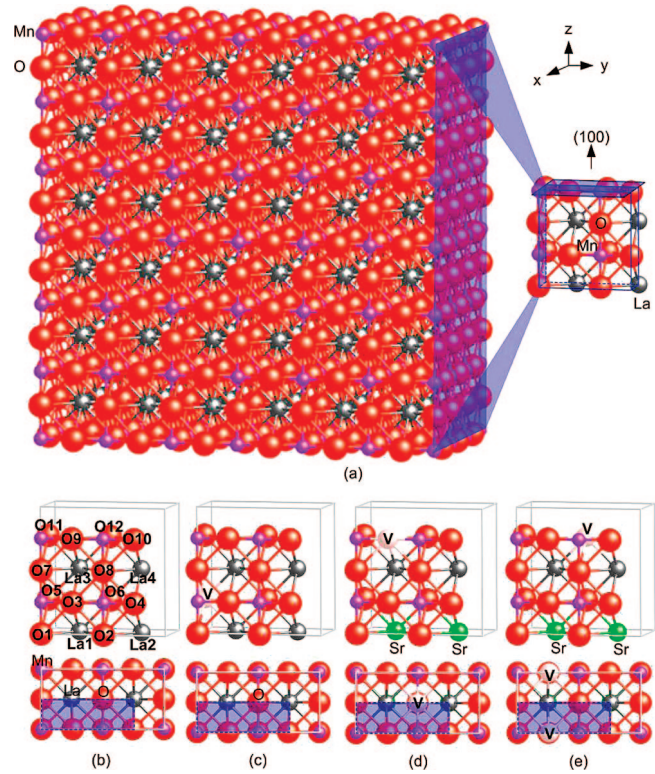

Figure 1. (a) Schematic representation of MnO-terminated $LaMnO_3$(100). Top and side views of (b) perfect $LaMnO_3$(100), (c) defective $LaMnO_3$(100), (d), and (e) $La_{0.5}Sr_{0.5}MnO_{2.75}$(100) surface models (**LSM1** and **LSM2**, respectively). Dashed rectangles and **V** denote a supercell and an oxygen vacancy, respectively. For clarity, top views include the ions repeated on the boundaries in x and y directions.

$$\Delta E_{ads,O} = \{E[\text{product}] - 1/2E[O_2] \times N - E[\text{surface}]\}/N \quad (1)$$

where E[product] and E[surface] are the calculated electronic energies of adsorbed oxygen species on the surface and a clean surface, respectively, while $E[O_2]$ is that of the triplet ground state of O_2. N is the number of adsorbed oxygen atoms. To obtain more systematic information for perfect $LaMnO_3$, we constructed a double-sized surface in the x direction (see Figure 1a), and then we evaluated four different coverages of 1/12, 1/6, 1/4, and 1/3 ML as illustrated in Figure S1. Shown in Figure 2 is a correlation curve of the adsorption energies on the two $LaMnO_3$ surface models of different sizes as a function of surface coverage. The linear correlation implies the insensitivity of adsorption energies predicted to the sizes of surface models, implying that the small surface model is adequate for the study of oxygen−surface interactions using periodic DFT calculations.

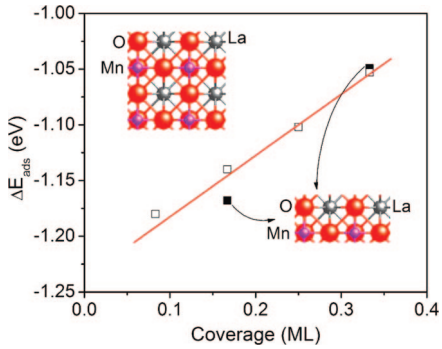

Figure 2. Adsorption energies as a function of coverage on MnO-terminated $LaMnO_3$(100). Adsorption energies were calculated according to eq 1. The solid line is fitted using the linear-squared method.

3.2. Interactions of O_2 on Sr-Doped $LaMnO_3$. The defect structures of $La_{1-x}Sr_xMnO_{3\pm\delta}$ are strongly dependent on partial pressure of oxygen and temperature.[32,33] Thus, to carry out kinetic and mechanistic studies, we constructed only a simplified model ($La_{0.5}Sr_{0.5}MnO_{2.75}$, **LSM50**) by substituting two La^{3+} by two Sr^{2+} in $LaMnO_3$, resulting in a doubly charged oxygen vacancy. We first generated defective $LaMnO_3$ structures by removing oxygen ions from the perfect $LaMnO_3$ surface model (see Figure 1b), providing the oxygen-vacancy formation energy, $\Delta E^f_{V_O} = E$[defective] + 1/2E[O_2] − E[perfect], where E[defective], E[O_2], and E[perfect] are the electronic energies of defective $LaMnO_3$, triplet O_2, and perfect $LaMnO_3$. As summarized in Table S1 in the Supporting Information, the configuration after removing **O5** (see Figure 1b and 1c) is energetically most stable among the 12 configurations. Next, we constructed Sr-doped $LaMnO_3$ surfaces (**LSM50**) based on the updoped surface model ($LaMnO_3$, see Figure 1b). We found that replacing the two bottom layer La^{3+} ions (**La1** and **La2**, see Figure 1b) by divalent Sr^{2+} ions gives the most stable structure by following an energy minimization process. Our calculations give a bulk lattice constant of 3.791 Å for the Sr-doped $LaMnO_3$ supercell containing 2 La, 2 Sr, 4 Mn, and 11 O ions. We did not find any significant symmetry change of the Sr-doped $LaMnO_3$ structure after a full optimization. To examine the effect of oxygen vacancies for O_2−surface interactions, even though configuration **O5** is more stable than configurations **O12** and **O9**, we applied the latter ones for generating **LSM50** surface models (**LSM1** and **LSM2**, respectively). Figure 1d and 1e shows **LSM50** which we used for characterizing the interactions between oxygen and surfaces. Similar to the O_2 interactions with perfect $LaMnO_3$, we carried out slab-model calculations by placing O_2 at Mn ions on the two surface models **LSM1** and **LSM2**. Figures S2 and S3 illustrate optimized oxygen species on the cathode materials with various configurations, while Tables S2 compiles their energetics and geometrical parameters. We assigned the molecularly adsorbed species as super- or peroxo-like structures based on their geometries, an end-on or a parallel configuration to the surface, respectively. As compiled in Table 1, it is clearly shown that the adsorption including dissociated configurations on **LSM50** is stronger than that on the perfect $LaMnO_3$, indicating that oxygen vacancies affect the adsorption. The adsorption on **LSM1** and **LSM2** surfaces exhibits that the oxygen-vacancy location alters O_2−surface interactions in terms of energetics and geometries. Interestingly, superoxo-like **super-lsm1** is slightly more stable than peroxo-like **per-lsm1** (see Table 1) on **LSM1**, which is different from O_2−$LaMnO_3$ interactions. To ascertain that **super-lsm1** is more stable than **per-lsm1**,[34] we used double-sized surface models in x and y directions (see Figure 1a), leading only to a slight change in the adsorption energies with the same trend.[34]

3.3. Mechanistic Studies for Oxygen Interactions on $LaMnO_3$ and $La_{0.5}Sr_{0.5}MnO_{2.75}$. Before performing the NEB calculations[20,21] to construct plausible reaction pathways on the model surfaces, we examined the charge-density change for the superoxo- and peroxo-like configurations compiled in Table 1. The estimated effective charges by using the Bader analysis code[22,23] show charge transfer between adsorbed oxygen species and the surface. Interestingly, it was found that the amounts of electrons transferred from the adsorbent to the adsorbate are not proportional to the adsorption energies. For example, although the peroxo-like structure is slightly less stable than the superoxo-like configuration on **LSM1**, the effective charge of the peroxo-like species is more negative than that of the superoxo-like species. While −0.38 |e| of **super-lsm1** is transferred from the **LSM1** surface through the interaction, −0.65 |e| is transferred to **per-lsm1** in the bond formation with the adsorption energies of −1.36 versus −1.20 eV, respectively. The charge-density change clearly demonstrates that more charge transfer on **LSM1** and **LSM2** occurs than on the perfect $LaMnO_3$ due to the presence of oxygen vacancies attributable to Sr doping (see the sum of effective charges in Figure 3). While NEB calculations have been successfully used to predict reaction pathways for other cases (see Scheme 1), we are unable to predict the "direct" reaction pathway for the transformation from the peroxo-like species (i.e., **per-lm** and **per-lsm1**) to the dissociation products (i.e., **diss-lm** and **diss-lsm1**) in this case because the peroxo-like species isomerizes to the superoxo-like species. As a result, we examined only the mechanistic steps up to the formation of the superoxo-like species. As illustrated in Figures 4−6, we constructed the potential energy profiles on the basis of energetically favorable configurations (see Table 1). To simulate the molecular adsorption on Mn ions and direct incorporation into the lattice, an oxygen molecule was placed in the vacuum space with a distance of ∼5.0 Å from the top layer of each surface model to guarantee no initial interaction of O_2 with the surfaces.

On the Perfect $LaMnO_3$ Surface. As O_2 approaches the Mn cation of the substrate, the total energy decreases and forms the **super-lm** intermediate with an exothermicity of 0.55 eV without an intrinsic barrier (see Figure 4). Next, **super-lm** dissociates to produce two oxygen atoms with an exothermicity of 2.10 eV after overcoming a reaction barrier of 0.45 eV at **ts-lm**. As mentioned, we found that the superoxo-like **super-lm** intermediate can convert to the peroxo-like **per-lm** intermediate with no barrier.

On the Sr-Doped $LaMnO_3$ Surfaces. Similar to the perfect $LaMnO_3$ surface, we carried out a mechanistic study for the molecular adsorption pathway at the **LSM50** surfaces. As depicted in Figure 5, for the interaction between O_2 and the **LSM1** surface, the first step is the formation of the superoxo-like **super-lsm1** intermediate with an exothermicity of 1.36 eV. From **super-lsm1**, **diss-lsm1** can be produced by overcoming a reaction barrier of 0.36 eV, which is much lower than that on the perfect $LaMnO_3$ (∼0.45 eV). The dissociated oxygen species is then incorporated into the doubly charged oxygen vacancy ($V_O^{\bullet\bullet}$), forming **inc-a1** or **inc-b1** with the same exothermicity of 3.90 eV. The adsorbed oxygen species on **inc-a1** can further diffuse to the Mn ion on **inc-b1** by overcoming a barrier of 2.09 eV. The oxygen species incorporated into the lattice can diffuse away by the hopping mechanism. We found that a bulk diffusion barrier using our $La_{0.5}Sr_{0.5}MnO_{2.75}$ model is ∼4.0 eV, which is in good agreement with an experimental value of 3.76

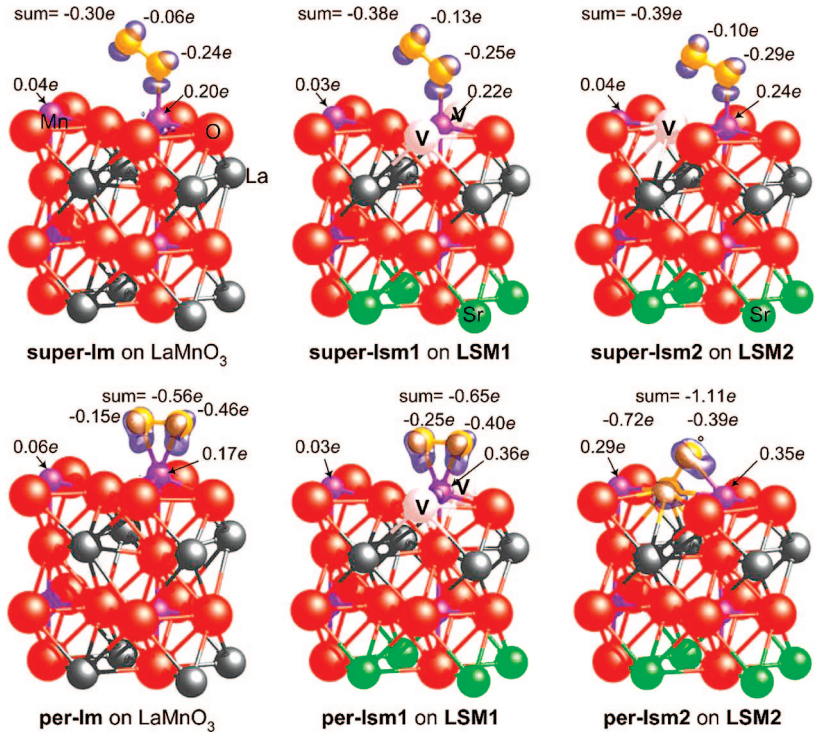

Figure 3. Illustration of charge-density changes and atomic charges for typical oxygen species on perfect and Sr-doped $LaMnO_3$. $\Delta\rho_{diff}$ isosurfaces were calculated at 0.0002 e/Å^3. Atomic charges are relative to those of the reactants. **V** denotes an oxygen vacancy.

TABLE 1: Summary of Adsorption Energies and Geometrical Parameters of Adsorbed Oxygen Species on the Perfect and Sr-Doped $LaMnO_3$ Surfaces

species	adsorption energies (eV)[a]	r(O−O) (Å)	r(O−Mn)[b] (Å)	υ(O−O) (cm^{-1})
$LaMnO_3$				
$LaMnO_3 + O_2$	0.00			
per-lm	−0.80 [−0.73]	1.377	2.184, 2.188	931
super-lm	−0.55 [−0.52]	1.296	1.875	1211
diss-lm	−2.10 [−2.02]		1.683, 1683	
$La_{0.5}Sr_{0.5}MnO_{2.75}$ (**LSM1**)				
LSM1 + O_2	0.00			
per-lsm1	−1.20 [−1.19]	1.386	1.824, 1.828	1033
super-lsm1	−1.36 [−1.34]	1.296	1.839	1236
diss-lsm1	−2.23 [−2.20]		1.598, 1600	
inc-a1	−3.90		1.599	
inc-b1	−3.90		1.579	
inc-c1	−2.06	1.467[c]		
$La_{0.5}Sr_{0.5}MnO_{2.75}$ (**LSM2**)				
LSM2 + O_2	0.00			
per-lsm2	−2.47	1.457		incorporated
super-lsm2	−1.18	1.304	1.853	
inc-a2	−3.85	1.460[b]	1.599	
inc-c2				

[a] The energies in brackets are zero-point energy (ZPE) corrected. [b] The shortest distance between an adsorbed oxygen species and an Mn ion. [c] The distance of an adsorbed oxygen (O_{ads}) species and an incorporated oxygen ($O_{lattice}$) species.

± 0.33 eV.[4,35] In addition to the molecular adsorption, oxygen molecules can directly be incorporated into oxygen vacancies via **ts3-lsm1**, producing **inc-c1** with an exothermicity of 2.06 eV. In the NEB calculation of the direct incorporation into the lattice, the coordinate of O_2 in the z direction was fixed. One oxygen species (O_{ads}) of **inc-c1** is vertically connected to the incorporated oxygen in the lattice ($O_{lattice}$) with an $O_{ads}-O_{lattice}$ distance of 1.467 Å. The adsorbed oxygen species can diffuse to the Mn ion of **inc-b1** with no barrier. To examine how the locations of oxygen vacancies influence the adsorption energies and reaction mechanisms, we studied the mechanism of the interactions between O_2 and the **LSM2** surface. As illustrated in Figure 6, similar to the O_2 adsorption on a perfect $LaMnO_3$ and **LSM1**, an oxygen molecule adsorbs on Mn ions (**super-lsm2**) with an exothermicity of 1.18 eV. Because of the location of an oxygen vacancy between two Mn ions on the surface, one of the oxygen species of the **super-lsm2** intermediate is directly incorporated in the lattice with no barrier, producing **inc-a2** with an exothermicity of 3.85 eV. An extensive search to locate a transition state for a direct dissociative pathway using

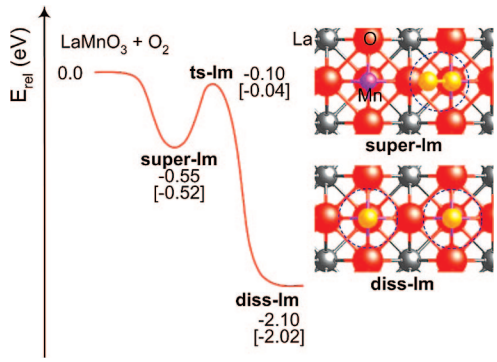

Figure 4. Potential energy profile and top views of an intermediate state and products for O_2−$LaMnO_3$ interactions. Dashed circles represent adsorbed oxygen species on the surface. Relative energies in brackets are (ZPE)-corrected.

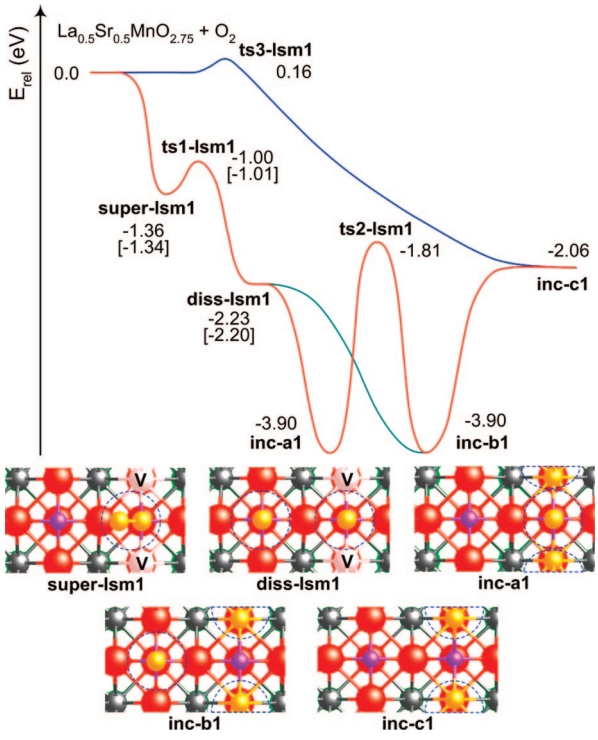

Figure 5. Potential energy profiles and top views of an intermediate state and products for O_2−$La_{0.5}Sr_{0.5}MnO_{2.75}$ (**LSM1**) interactions. **V** denotes an oxygen vacancy. Dashed circles and **V** represent adsorbed oxygen species and an oxygen vacancy on the surface, respectively. Relative energies in brackets are (ZPE)-corrected.

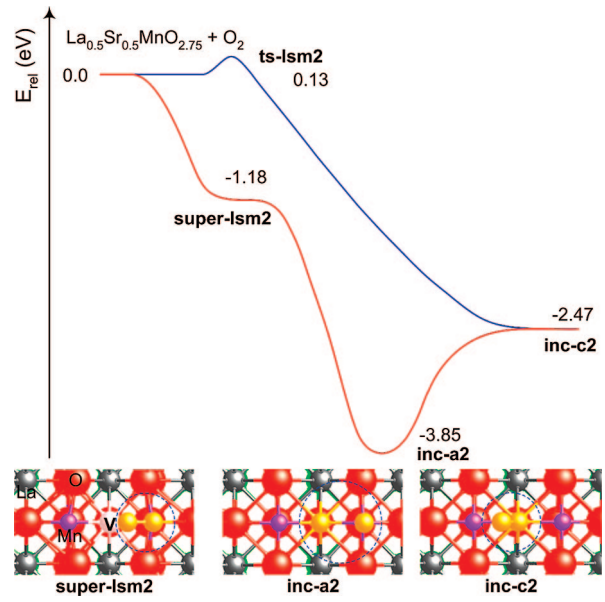

Figure 6. Potential energy profile for O_2−$La_{0.5}Sr_{0.5}MnO_{2.75}$ (**LSM2**) interactions. Dashed circles and **V** represent adsorbed oxygen species and an oxygen vacancy on the surface, respectively.

diss-lsm2 (see Table S2 and Figure S3) was unsuccessful; thus, we did not consider the product for our mechanistic studies. Our adsorption-energy calculations show that molecularly adsorbed oxygen species with the peroxo-like configuration on **LSM2**, similar to **per-lsm1** on **LSM1**, may not exist, because it is directly incorporated into the oxygen vacancy.[36] In a manner similar to the case in which we examined the direct incorporation into the lattice in the **LSM1** surface, we found a 0.13 eV barrier at **ts-lsm2**. The vertically connected oxygen species (O_{ads}) to the incorporated oxygen in the lattice ($O_{lattice}$) can further diffuse to **inc-c2** with no barrier.

3.4. Prediction of Rate Constants for O_2 Interactions on $LaMnO_3$ and $La_{0.5}Sr_{0.5}MnO_{2.75}$. As summarized in Scheme 2, the adsorption step of O_2−cathode interactions can occur without a barrier (**vts**, variational transition state). Thus, we performed the CVTST calculations[27] to locate their transition states based on the maximum Gibbs free energy criterion at each temperature. For example, a variational potential energy curve was mapped out using the NEB method along the MEP with eight images (see Figure S4). The MEP curve for the adsorption process of O_2−$La_{0.5}Sr_{0.5}MnO_{2.75}$ (**LSM1**) forming **super-lsm1** was obtained by varying the shortest bond distance of O_2 and the substrate from its equilibrium value (1.839 Å, see Table 1) up to 5.0 Å. This means that the adsorption starts from the distance of 5.0 Å, from the surface (Mn ion) to the shortest oxygen from the surface, until O_2 adsorbs on the Mn ion, leading to the elongation of the O−O distance from 1.244 to 1.296 Å, while their calculated O−O stretching modes are 1558 and 1236 cm^{-1}, respectively. Table S3 compiles the predicted energies and molecular parameters applied for predicting maximum ΔG (T,s) at each temperature. Because we assumed that the surface may not be altered too much during O_2−surface interactions, the substrate for each image has the same vibrational frequencies as summarized in Table S4. The calculated energies were fitted to the Morse potential energy function, $E(R) = D_e[1 - \exp(-\beta(R - R_0))]^2$, with $D_e = 1.36$ eV, $\beta = 3.67$ $Å^{-1}$, and $R_0 = 1.839$ Å, where D_e is the dissociation energy without ZPE corrections, R is the reaction coordinate, and R_0 is the equilibrium O−surface bond distance. Our CVTST calculations demonstrate that transition states may be located near the distance of ~3.21 Å in the temperature range of 873−1273 K (see **vts-lsm1** in Table S3). We assumed the adsorption process for O_2−$LaMnO_3$ interactions have loose transition states (see **vts-lm** in Table S3) similar to those of O_2−**LSM1** interactions. Using ZPE-corrected energetics summarized in Table 1, we calculated rate constants as implemented in the ChemRate program.[29] For the kinetic predictions related to $La_{0.5}Sr_{0.5}MnO_{2.75}$, we examined the O_2 interactions only on **LSM1** due to the nonexistence of a dissociation barrier on **LSM2**. The predicted rate constants for the O_2 adsorption process on $LaMnO_3$ and **LSM1** at $T = 873$−1273 K can be represented, respectively, by $k_{ads,lm} = 1.30 \times 10^2 T^{2.36}$ cm^3 s^{-1} and $k_{ads,lsm} = 3.46 \times 10^2 T^{2.52}$ cm^3 s^{-1}, where the rate constants are related to the rate equation,[37−41] $d[X]_{surf}/dt = k_i(\theta/A_s)[X]_g$,

SCHEME 2: Reaction Pathways for the O_2 Reduction on (a) $LaMnO_3$ and (b) $La_{0.5}Sr_{0.5}MnO_{2.75}$[a]

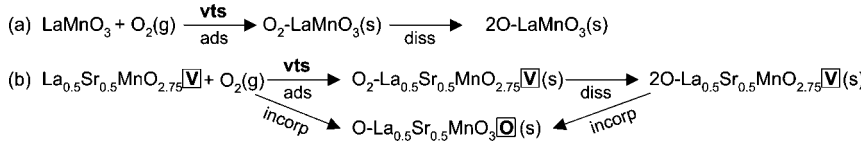

[a] (g), (s), **vts**, and **V** denote gas, surface, variational transition state, and oxygen vacancy, respectively, while "ads", "diss", and "incorp" are adsorption, dissociation, and incorporation, respectively.

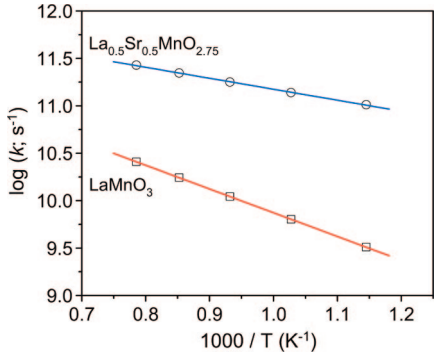

Figure 7. Comparison of predicted rate constants for the dissociation process of O_2 on the perfect $LaMnO_3$ and $La_{0.5}Sr_{0.5}MnO_{2.75}$ (**LSM1**). Solid lines are fitted using the linear-squared method.

which has the units of a flux, molecule cm^{-2} s^{-1}. In the rate equation, θ represents the fraction of available surface sites, A_s is the surface area, and $[X]_g$ is the gas-phase concentration of O_2 in molecules cm^{-3}. Figure 7 shows the dissociation of adsorbed oxygen species on $La_{0.5}Sr_{0.5}MnO_{2.75}$ dominates over the temperature range studied, leading to the expression of $k_{diss,lsm} = 2.15 \times 10^{12}$ exp(−0.23 eV/*RT*) s^{-1} at $P = 1$ atm and $T = 873-1273$ K. The desorption is too slow to compete with the dissociation on the **LSM1** surface; its contribution to the reaction is thus negligible ($k_{des,lsm} = 3.80 \times 10^{12}$ exp(−1.03 eV/*RT*) s^{-1}). However, the desorption of adsorbed oxygen species on the perfect $LaMnO_3$ can compete with its dissociation on account of their comparable reaction barriers relative to **super-lm** (~0.52 and ~0.48 eV, respectively). The predicted rate constants on the perfect $LaMnO_3$ can be expressed: $k_{diss,lm} = 2.35 \times 10^{12}$ exp(−0.50 eV/*RT*) s^{-1} and $k_{des,lm} = 6.23 \times 10^{12}$ exp(−0.57 eV/*RT*) s^{-1}. Our rate-constant predictions along with the mechanistic studies verify that oxygen vacancies influence O_2 kinetics on SOFC cathodes.

3.5. Potential Applications to Continuum Modeling. In this section, we briefly discuss how the predicted rate constants can be employed for kinetic simulations of the operation of a practical SOFC system by integration with continuum modeling. Both types of modeling can separately provide important insights, on different length scales, into the electrochemical and transport processes. When the two approaches are used together, the combination will make for a powerful multiscale modeling approach to illustrate the kinetic processes more clearly.

Continuum models,[42−51] specifically numerical models conforming to catalyst geometry such as those we have developed,[42−44] can capture complicated kinetic and transport processes and apply predictions on a scale applicable to thin film, patterned, and other electrode configurations. These models wrap kinetic processes into phenomenological rate equations, sufficiently capturing the critical features in a manner simple enough to apply to the relatively large length scales. Rational design of novel cathodes is aided because the complicated effects of experimental variables and the resulting concentration fields are taken into account when determining electrochemical response. Materials and geometric configurations may be screened by a proper implementation of numerical continuum models.

The continuum modeling requires phenomenological parameters to assign rates to the various kinetic processes under consideration. One such set of parameters includes mobility of various charge-carriers, for instance, that of oxygen vacancies, u_v, and adsorbed surface species, u_{O-^s}. Another set includes rate constants for various reactions such as oxygen adsorption and incorporation, k_{ads}^0 and k_{inc}^0, respectively. Also included are estimates of concentration, such as equilibrium coverage of adsorbed species, θ_0, and equilibrium content of oxygen vacancies, c_v^0. We are in the process of implementing estimated rate constants and using quantum chemical calculations to estimate the parameters u_{O-^s}, c_v^0, and u_v^m for LSM compositions of interest.

Some parameters may be determined on the basis of well-established techniques and can be verified or augmented by quantum chemical modeling. For instance, SIMS can measure the surface exchange coefficient, k^*, and tracer diffusivity, D^* (e.g., for LSM[4,35] and $La_{1-x}Sr_xCo_{1-y}Fe_yO_{3-\delta}$[52−54]). The former parameter may be related directly to k_{inc}^0 or k_{ads}^0, depending on which step is rate-limiting, whereas the latter may be related to vacancy mobility, u_v. The value of c_v^0 can be estimated by weight loss in conjunction, if necessary, with a defect model if uncertainty exists (e.g., LSM at high pO_2).[55,56] Ideally, first-principles prediction agrees with the reported experimental value; alternatively, it can enhance the interpretation of experimental data, leading to model refinement and eventual agreement.

Quantum chemical calculations are of greatest value to continuum modeling in the case where few or poor experimental techniques exist, including finding many surface parameters, such as θ_0 and u_{O-^s}, as well as elucidating the breakdown of important reactions into elementary steps (e.g., the nature of the adsorption process when incorporation is rate limiting, the subject of this Article). An example of such a connection may be found in the phenomenological equation[43] for the rate of dissociative chemisorption of oxygen species onto an LSM surface (see eq 2). Here, k_{ads}^0 is a phenomenological rate constant in the units of mol m^{-2} s^{-1}, equal to the rate of adsorption/desorption at equilibrium. This parameter is tied to more fundamental rate constants, $\vec{k}_{ads}$ and $\overleftarrow{k}_{des}$, describing forward (adsorption) and backward (desorption) processes, respectively, both of which are proportional to a temperature term.

$$r_{ads} = k_{ads}^0 \left[\frac{P_{O_2}^{1/2}}{P_{O_{2,0}}^{1/2}} \frac{(1-\theta)}{(1-\theta_0)} \exp\left(-\frac{\alpha F}{RT}\Delta\chi_s\right) - \frac{c_h}{c_{h,0}} \frac{\theta}{\theta_0} \exp\left(\frac{(1-\alpha)F}{RT}\Delta\chi_s\right) \right] \quad (2)$$

Few of these parameters are readily accessible by experiment if adsorption is not the macroscopic rate-limiting process. However, in some specific circumstances such as near TPBs, adsorption may be critical, and an estimate of the parameters is important.

While the work presented in this Article is for very specific surface configurations, quantum chemical calculations can nevertheless provide estimates for polycrystalline materials with perhaps a variety of exposed crystalline faces. Such predictions provide general guidance for generic surfaces, an improvement over what is available experimentally.

4. Conclusions

The interactions between oxygen molecules and Sr-doped or undoped $LaMnO_3$ were examined using periodic DFT calculations and statistical-theory methods. Results suggest that the stability of the molecularly adsorbed and dissociated oxygen species depends on surface orientation and defects of the cathode materials. It is also predicted that the presence of oxygen vacancies on the surface enhances the dissociation rate of adsorbed oxygen species because of a lower dissociation barrier on $La_{0.5}Sr_{0.5}MnO_{2.75}$ (0.33 eV) than on $LaMnO_3$ (0.48 eV). The estimated rate constants on $LaMnO_3$ (**lm**) and $La_{0.5}Sr_{0.5}MnO_{2.75}$ (**lsm**) can be expressed as: $k_{\mathrm{diss,lm}} = 2.35 \times 10^{12} \exp(-0.50\ \mathrm{eV}/RT)\ \mathrm{s}^{-1}$ and $k_{\mathrm{diss,lsm}} = 2.15 \times 10^{12} \exp(-0.23\ \mathrm{eV}/RT)\ \mathrm{s}^{-1}$, respectively, at $P = 1$ atm and $T = 873-1273$ K. While the predicted rate constants cannot be directly compared to available surface oxygen exchange coefficients (k^*),[5] a profound understanding of the effect of temperature and pressure on the kinetics of surface reactions in molecular scale may provide vital insight to the design of more efficient cathode materials for SOFCs.

Acknowledgment. We are grateful for the financial support provided by the DOE-NETL University Coal Program (Grant No. DE-FG26-06NT42735) and DOE Basic Energy Science (Grant No. DE-FG02-06ER15837). We acknowledge the use of CPUs from the National Center for High-performance Computing, Taiwan, supported by INER under contract no. NL 940251. This work was also partly performed using the MSCF in EMSL at Pacific Northwest National Laboratory (PNNL), a national scientific user facility sponsored by the U.S. DOE and OBER. M.C.L. also wants to acknowledge the support from the MOE ATP program, Taiwan Semiconductor Manufacturing Co. for the TSMC Distinguished Professorship, and Taiwan National Science Council for the Distinguished Visiting Professorship at the Center for Interdisciplinary Molecular Science, National Chiao Tung University, Hsinchu, Taiwan. M.E.L. appreciates financial support through a National Science Foundation graduate research fellowship. Y.C. acknowledges fruitful discussions on the DFT calculations and on the oxygen reduction reaction in SOFCs with Dr. De-en Jiang and Dr. Shizhong Wang, respectively.

Supporting Information Available: Detailed information on energetics, molecular parameters, and optimized geometries. This material is available free of charge via the Internet at http://pubs.acs.org.

References and Notes

(1) Steele, B. C. H.; Heinzel, A. *Nature (London)* **2001**, *414*, 345–352.
(2) Xia, C.; Liu, M. *Adv. Mater.* **2002**, *14*, 521–523.
(3) Chater, R. J.; Carter, S.; Kilner, J. A.; Steele, B. C. H. *Solid State Ionics* **1992**, *53−56*, 859–867.
(4) De Souza, R. A.; Kilner, J. A. *Solid State Ionics* **1998**, *106*, 175–187.
(5) De Souza, R. A. *Phys. Chem. Chem. Phys.* **2006**, *8*, 890–897.
(6) It is noted that a different phenomenological parameter k^δ can be obtained from conductivity relaxation experiments. The differences between k^* and k^δ can be found in detail in ref 7.
(7) Maier, J. *Solid State Ionics* **1998**, *112*, 197–228.
(8) Liu, M.; Hu, H. *J. Electrochem. Soc.* **1996**, *143*, L109–112.
(9) Minh, N. Q.; Takahashi, T. *Science and Technology of Ceramic Fuel Cells*; Elsevier: Amsterdam, 1995.
(10) Choi, Y.; Mebane, D. S.; Lin, M. C.; Liu, M. *Chem. Mater.* **2007**, *19*, 1690–1699.
(11) Choi, Y.; Lin, M. C.; Liu, M. *Angew. Chem, Int. Ed.* **2007**, *46*, 7214–7219.
(12) Kotomin, E. A.; Mastrikov, Y. A.; Heifets, E.; Maier, J. *Phys. Chem. Chem. Phys.* **2008**, *10*, 4644–4649.
(13) Kresse, G.; Hafner, J. *Phys. Rev. B* **1993**, *47*, 558–561.
(14) Kresse, G.; Furthmüller, J. *Phys. Rev. B* **1996**, *54*, 11169–11186.
(15) Blöchl, P. E. *Phys. Rev. B* **1994**, *50*, 17953–17979.
(16) Perdew, J. P.; Burke, K.; Ernzerhof, M. *Phys. Rev. Lett.* **1996**, *77*, 3865.
(17) Monkhorst, H. J.; Pack, J. D. *Phys. Rev. B* **1976**, *13*, 5188–5192.
(18) Evarestov, R. A.; Kotomin, E. A.; Mastrikov, Y. A.; Gryaznov, D.; Heifets, E.; Maier, J. *Phys. Rev. B* **2005**, *72*, 214411.
(19) Mastrikov, Y. A.; Heifets, E.; Kotomin, E. A.; Maier, J. *Surf. Sci.* **2009**, *603*, 326–335.
(20) Mills, G.; Jónsson, H.; Schenter, G. *Surf. Sci.* **1995**, *324*, 305–337.
(21) Henkelman, G.; Uberuaga, B. P.; Jónsson, H. *J. Chem. Phys.* **2000**, *113*, 9901.
(22) Henkelman, G.; Arnaldsson, A.; Jónsson, H. *Comput. Mater. Sci.* **2006**, *36*, 354–360.
(23) http://theory.cm.utexas.edu/bader/.
(24) Bader, R. F. W.; Beddall, P. M. *J. Chem. Phys.* **1972**, *56*, 3320.
(25) Bader, R. F. W. *Atoms in Molecules - A Quantum Theory*; Clarendon Press: Oxford, 1994.
(26) Laidler, K. J. *Chemical Kinetics*, 3rd ed.; Harper and Row: New York, 1987.
(27) Truhlar, D. G. *The Reaction Path in Chemistry: Current Approaches and Perspectives*; Kluwer Academic Publishers: The Netherlands, 1995.
(28) Zhu, R. S.; Wang, J. H.; Lin, M. C. *J. Phys. Chem. C* **2007**, *111*, 13831–13838.
(29) Mokrushin, V.; Bedanov, V.; Tsang, W.; Zachariah, M. R.; Knyazev, V. D. *ChemRate*; version 1.19, 2002.
(30) Experimental values are 3.879 and 3.889 Å, see: Jena, H.; GovindanKutty, K. V.; Kutty, T. R. *J. Alloys Compd.* **2003**, *350*, 102. Arima, T.; Tokura, Y. *J. Phys. Soc. Jpn.* **1995**, *64*, 2488.
(31) Takeda, Y.; Kanno, R.; Noda, M.; Tomida, Y.; Yamamoto, O. *J. Electrochem. Soc.* **1987**, *134*, 2656–2661.
(32) Kuo, J. H.; Anderson, H. U.; Sparlin, D. M. *J. Solid State Chem.* **1989**, *83*, 52–60.
(33) Mizusaki, J.; Mori, N.; Takai, H.; Yonemura, Y.; Minamiue, H.; Tagawa, H.; Dokiya, M.; Inaba, H.; Naraya, K.; Sasamoto, T.; Hashimoto, T. *Solid State Ionics* **2000**, *129*, 163–177.
(34) The adsorption-energy change on **LSM1** is 0.16 eV according to E[**per-lsm1**]$-$ E[**super-lsm1**]. We found a slight adsorption-energy change with the same trend on the surfaces double-sized in x and y directions (0.07 and 0.14 eV, respectively). This is different from our previous studies using LaMnO-terminated (110) surfaces (ref 11), implying surface orientations influence the energetics.
(35) De Souza, R. A.; Kilner, J. A. *Solid State Ionics* **1999**, *126*, 153–161.
(36) We located peroxo-like configurations on **LSM2** as summarized in Table S4 and Figure 6.
(37) Weinberg, W. H. In *Dynamics of Gas-Surface Interactions*; Rettner, C. T., Ashfold, M. N. R., Eds.; The Royal Society of Chemistry: Cambridge, 1991; pp 171−219.
(38) Pitt, I. G.; Gilbert, R. G.; Ryan, K. R. *J. Phys. Chem.* **1994**, *98*, 13001–13010.
(39) Xu, S. C.; Irle, S.; Musaev, D. G.; Lin, M. C. *J. Phys. Chem. B* **2006**, *110*, 21135–21144.
(40) Xu, S. C.; Irle, S.; Musaev, D. G.; Lin, M. C. *J. Phys. Chem. C* **2007**, *111*, 1355–1365.
(41) Chen, H.-L.; Ju, S.-P.; Chen, H.-T.; Musaev, D. G.; Lin, M. C. *J. Phys. Chem. C* **2008**, *112*, 12342–12348.
(42) Lynch, M. E.; Mebane, D. S.; Liu, Y.; Liu, M. *J. Electrochem. Soc.* **2008**, *155*, B635–B643.
(43) Mebane, D. S.; Liu, M. *J. Solid State Electrochem.* **2006**, *10*, 575–580.
(44) Mebane, D. S.; Liu, Y.; Liu, M. *J. Electrochem. Soc.* **2007**, *154*, A421–A426.
(45) Fleig, J. *Annu. Rev. Mater. Res.* **2003**, *33*, 361–382.
(46) Mitterdorfer, A.; Gauckler, L. J. *Solid State Ionics* **1999**, *117*, 187–202.

(47) Mitterdorfer, A.; Gauckler, L. J. *Solid State Ionics* **1999**, *117*, 203–217.

(48) Kamata, H.; Hosaka, A.; Mizusaki, J.; Tagawa, H. *Solid State Ionics* **1998**, *106*, 237–245.

(49) Adler, S. B.; Lane, J. A.; Steele, B. C. H. *J. Electrochem. Soc.* **1996**, *143*, 3554–3564.

(50) Svensson, A. M.; Sunde, S.; Nisancioglu, K. *Solid State Ionics* **1996**, *86−88*, 1211–1216.

(51) Fleig, J. *Phys. Chem. Chem. Phys.* **2005**, *7*, 2027–2037.

(52) Benson, S. J.; Chater, R. J.; Kilner, J. A. *Proc. Electrochem. Soc.* **1998**, *97−24*, 596–609.

(53) Carter, S.; Selcuk, A.; Chater, R. J.; Kajda, J.; Kilner, J. A.; Steele, B. C. H. *Solid State Ionics* **1992**, *53−6*, 597–605.

(54) van Doorn, R. H. E.; Fullarton, I. C.; deSouza, R. A.; Kilner, J. A.; Bouwmeester, H. J. M.; Burggraaf, A. J. *Solid State Ionics* **1997**, *96*, 1–7.

(55) Mebane, D. S.; Liu, Y.; Liu, M. *Solid State Ionics* **2008**, *178*, 1950–1957.

(56) Poulsen, F. W. *Solid State Ionics* **2000**, *129*, 145–162.

JP811021P